

Journal of Biomedical Optics

SPIEDigitalLibrary.org/jbo

Investigation of a diffuse optical measurements-assisted quantitative photoacoustic tomographic method in reflection geometry

Chen Xu
Patrick D. Kumavor
Andres Aguirre
Quing Zhu

Investigation of a diffuse optical measurements-assisted quantitative photoacoustic tomographic method in reflection geometry

Chen Xu, Patrick D. Kumavor, Andres Aguirre, and Quing Zhu

University of Connecticut, Electrical and Computer Engineering Department, 371 Fairfield Road, Unit 2157, Storrs, Connecticut 06269-2157

Abstract. Photoacoustic tomography provides the distribution of absorbed optical energy density, which is the product of optical absorption coefficient and optical fluence distribution. We report the experimental investigation of a novel fitting procedure that quantitatively determines the optical absorption coefficient of chromophores. The experimental setup consisted of a hybrid system of a 64-channel photoacoustic imaging system with a frequency-domain diffused optical measurement system. The fitting procedure included a complete photoacoustic forward model and an analytical solution of a target chromophore using the diffusion approximation. The fitting procedure combines the information from the photoacoustic image and the background information from the diffuse optical measurements to minimize the photoacoustic measurements and forward model data and recover the target absorption coefficient quantitatively. 1-cm-cube phantom absorbers of high and low contrasts were imaged at depths of up to 3.0 cm. The fitted absorption coefficient results were at least 80% of their true values. The sensitivities of this fitting procedure to target location, target radius, and background optical properties were also investigated. We found that this fitting procedure was most sensitive to the accurate determination of the target radius and depth. Blood sample in a thin tube of radius 0.58 mm, simulating a blood vessel, was also studied. The photoacoustic images and fitted absorption coefficients are presented. These results demonstrate the clinical potential of this fitting procedure to quantitatively characterize small lesions in breast imaging. © 2012 Society of Photo-Optical Instrumentation Engineers (SPIE). [DOI: 10.1117/1.JBO.17.6.061213]

Keywords: absorption coefficient; photoacoustic tomography; reflection geometry; diffuse optical measurements; fitting procedure.

Paper 11381SSP received Jul. 19, 2011; revised manuscript received Jan. 9, 2012; accepted for publication Feb. 1, 2012; published online May 7, 2012.

1 Introduction

Photoacoustic tomography (PAT) takes advantage of the high optical absorption of blood-rich tumors and relatively low optical absorption of normal tissues in the near-infrared (NIR) optical spectrum to offer high-resolution and high-contrast images for up to a few centimeters in depth.^{1–10} PAT, therefore, has great potential to detect early-stage breast cancers.^{2,6,10} Oraevsky's group was one of the first to build a PAT system solely for breast imaging.^{6,11,12} However, conventional PAT can only provide the distribution of absorbed optical energy density, which is the product of optical absorption coefficient and optical fluence distribution. The absorbed energy density is clearly not the intrinsic functional parameter for breast cancer diagnosis, as it depends on the distribution of the external light illumination, which is a spatially varying function. In the past, our group developed a dual-modality system that uses the location information provided by PAT to guide diffuse optical tomography (DOT) for quantifying the absorption coefficient distribution of targets.^{13,14} This approach offers low-resolution DOT images and cannot take full advantage of the high resolution provided by the PAT images. Several groups have investigated the reconstruction of the absolute absorption coefficient distribution

from PAT images.^{15–22} Jiang et al.^{15–17} have used the finite element method to first recover the absorbed optical energy density, followed by the use of the photon diffusion equation to extract the absorption coefficient. Laufer et al.^{18,19} developed the spectrum technique to iteratively fit the chromophore concentration from measurements of photoacoustic signals acquired at different wavelengths. Other groups have introduced different methods to reconstruct optical absorption quantitatively, such as using sparse signal representation,²⁰ multiple optical sources,²¹ or acoustic spectra.²² In all of these methods, however, the importance of the background optical property is not emphasized, although it significantly affects the reconstructed quantitative PAT absorption coefficients. In this paper, we introduce a fitting procedure that uses diffuse optical measurements (DOM) to assist PAT in quantifying tissue-absorption coefficient. The PAT setup used is the reflection geometry because it offers more comfort and convenience to the patient during breast imaging. In Sec. 2 of this paper, the forward model, the fitting procedure, and the experimental system are introduced. In Sec. 3, the simulation and experimental results are presented. It will be shown that the reconstruction accuracy obtained is about 84% for a high contrast target and 88% for a low contrast target embedded in a highly scattering medium. Section 3 also discusses the sensitivities of this fitting procedure to the target parameters (radius and location) and background optical properties.

Address all correspondence to: Quing Zhu, University of Connecticut, Electrical and Computer Engineering Department, 371 Fairfield Road, Unit 2157, Storrs, Connecticut 06269-2157. Tel: +860 486 3344; E-mail: zhu@engr.uconn.edu

2 Methods

2.1 Forward Model

The complete forward model combines the model of light propagation through the scattering medium and the model of photoacoustic wave propagation. The photon diffusion equation is used to describe the fluence distribution inside the medium. The simple analytical expressions for fluence inside the target and background medium²³ are implemented in the model. The fluence inside the target, Φ_{in} , and background medium, Φ_{out} , are only related to background optical properties, target optical properties, and target position as:

$$\Phi_{out} = \frac{vS_0}{4\pi|r-r_s|} \exp(ik_{out}|r-r_s|) + \sum_{l,m} [A_{l,m}j_l(k_{out}r) + B_{l,m}n_l(k_{out}r)]Y_{l,m}(\theta, \phi), \quad (1a)$$

$$\Phi_{in} = \sum_{l,m} [C_{l,m}j_l(k_{in}r) + D_{l,m}n_l(k_{in}r)]Y_{l,m}(\theta, \phi). \quad (1b)$$

In Eqs. (1a) and (1b), $A_{l,m}$, $B_{l,m}$, $C_{l,m}$, and $D_{l,m}$ are coefficients. $j_l(x)$ and $n_l(x)$ are the spherical Bessel and Neumann functions, respectively, and $Y_{l,m}(\theta, \phi)$ is the spherical harmonics. k_{out} and k_{in} are the complex wave numbers of the background medium and target, respectively, and are related to their optical properties. As a result, the absorbed optical energy distribution (Q) can be determined and related to the background optical properties, target optical properties, and target position as well. The initial photoacoustic pressure wave induced by a short-pulsed laser is proportional to the absorbed optical energy density distribution and Gruneisen coefficient (Γ). The initial pressure, $p_0(r, \mu_a)$, and the subsequent acoustic wave, $p(r, t)$, can be expressed by the following equations:²⁴

$$p_0(r, \mu_a) = \Gamma Q(r, \mu_a), \quad (2a)$$

$$p(r, t) = \frac{1}{4\pi c} \frac{\partial}{\partial t} \int_{|\Delta r|=ct} \frac{p_0(r-\Delta r)}{ct} ds. \quad (2b)$$

From Eqs. (1) and (2), it can be seen that the simulated pressure signal is determined by the background optical properties, target optical properties, and the target position.

2.2 Fitting Procedure

The complete fitting procedure, described by a three-step process, is illustrated in Fig. 1. The first step is to obtain the background optical properties using the diffuse optical measurement system.²⁵ Since a probe with a flat surface was used for housing the ultrasound transducer, optical sources, and detectors, a semi-infinite geometry was a reasonable approximation for the optical measurements. The following set of linear equations were used to relate the calibrated amplitude $I_{\alpha\beta}$ and phase $\phi_{\alpha\beta}$ measured at the source-detector pair $\alpha\beta$, to the source-detector separation $\rho_{\alpha\beta}$ as,²⁶

$$\log(\rho_{\alpha\beta}^2 I_{\alpha\beta}) = -k_i \rho_{\alpha\beta}, \quad (3a)$$

$$\phi_{\alpha\beta} = k_r \rho_{\alpha\beta}, \quad (3b)$$

where k_r and k_i are the real and imaginary parts of the complex wave number, respectively. We leave the wave number as a variable and use the fitted k_r and k_i values to calculate the background scattering and absorption coefficients. The importance of background optical properties will be demonstrated in the next section. In the second step, the map of the absorbed optical energy density is reconstructed using the delay-and-sum algorithm.²⁷ The accurate location and radius of the target are read and used in the iteration in the next step. The third and last step is the inversion scheme to recover the absorption coefficient distribution from the photoacoustic measurements. Since the background optical properties and target position are determined in step 1 and step 2 above, the only unknown variables for the simulated pressure signal are the target optical properties. The object function (E) is defined as the difference between the experimental signal and the simulated signal, and is given as:

$$E = \sum [P_{Data}(\mu_{a,t}, \mu'_{s,t}) - P_{Sim}(\mu_{a,t}, \mu'_{s,t})]^2. \quad (4)$$

The optical properties of the target can be fitted using an iterative method to minimize the object function. The nonlinear

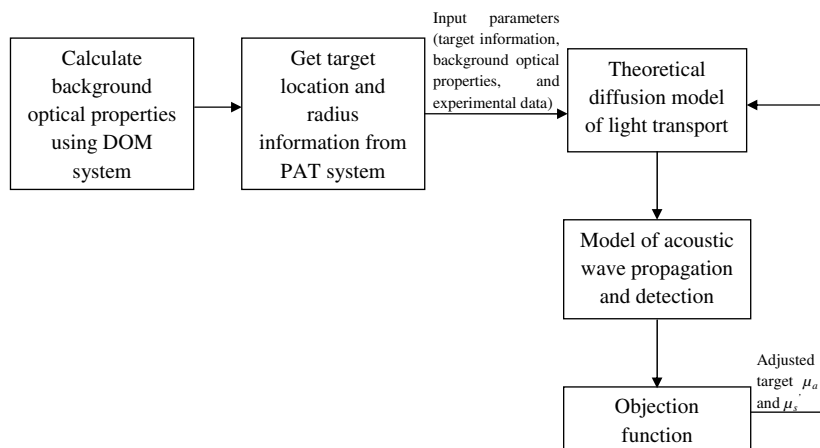


Fig. 1 Fitting procedure to quantitatively recover the target optical properties.

regression function *fminsearch*, used in the minimization procedure, is available in MATLAB. If the optical properties of the background are unknown, then a four-parameter fitting procedure (μ_a and μ_s' of the background medium, and μ_a and μ_s' of the target) is needed. In this case, the two-parameter fitting procedure can be modified to a four-parameter one as follows: (a) the first step in the three-step-procedure is skipped; (b) the target location information is determined in the second step as before; and (c) the object function in the third step is modified to incorporate μ_a and μ_s' of the background medium. This modified procedure hence allows the parameters, μ_a and μ_s' of the background medium, and μ_a and μ_s' of the target, to be fitted.

2.3 Experimental System and Phantom

Figure 2(a) shows the experimental configuration of the diffuse optical measurements-assisted (DOM) PAT system. A Ti:Sapphire (Symphotics TII, LS-2134) laser optically pumped by a Q-switched Nd:YAG laser (Symphotics-TII, LS-2122), delivered 10-ns pulses at 15 Hz and 750 nm. The laser output was coupled into two 1000-micron step-index input fibers (Thorlabs, BFL48-1000) using a convex lens and circular beamsplitter

arrangement as shown in the figure. The convex lens, which has 99% transmittance at 750-nm wavelength, has a focal length of 20 cm and focuses the light into the pair of fibers that are placed at its focal point. The beam splitter was used to split the incoming beam into two beams, one for each fiber. It was measured to have a 60% transmitting and 36% reflecting split ratio for horizontally polarized light at the 750 nm that was used for the experiment. The overall coupling efficiency of the setup (including the losses in the lens and beam splitter) was about 85%, and the total output energy was about 18 mJ per pulse. The two output ends of the fibers were then mounted on opposite (longitudinal) sides of a low-frequency linear ultrasound transducer described below and used for photoacoustic imaging.

A low-frequency ultrasound transducer was employed to maximize the sensitivity for photoacoustic signal detection. The ultrasound transducer manufactured by Vernon (France) had 64 elements with 0.85-mm pitch. The center frequency of the transducer was 1.3 MHz with a 6-dB response from 500 to 1800 kHz. An integrated acoustic lens with 2.5-cm focal length increased the sensitivity at imaging depths for which the optical fluences were low. The photoacoustic signals

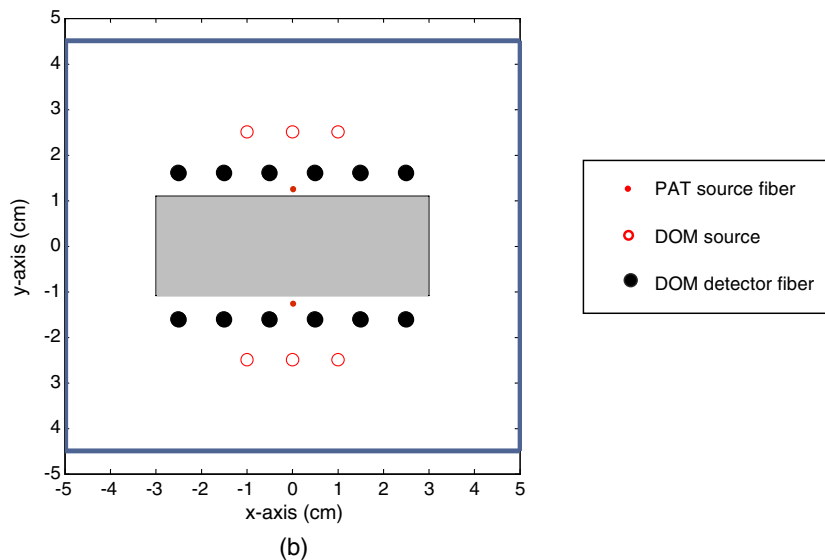
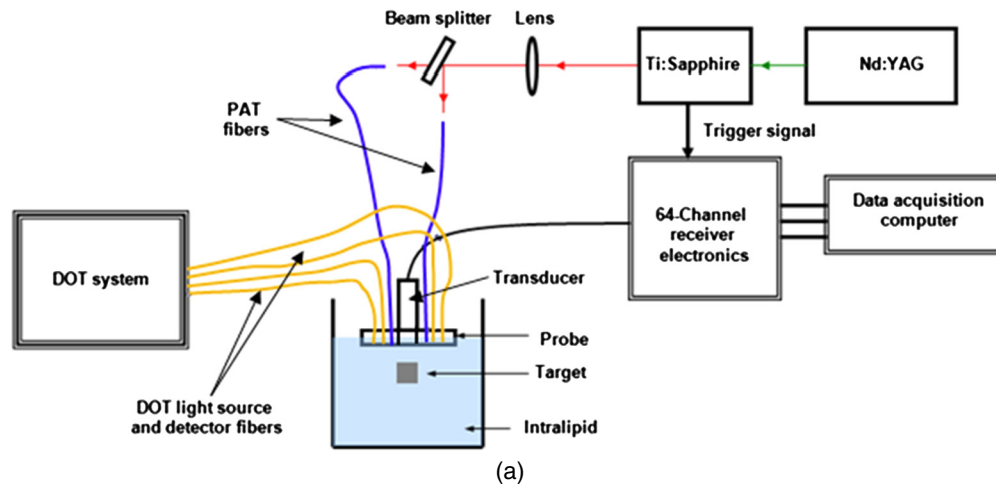


Fig. 2 (a) Experimental configuration of diffuse-optical-measurement-assisted PAT system; (b) probe geometry used for simulation and phantom experiments.

from the 64-array elements were individually amplified by 60 dB using receiver electronics designed and constructed by our group and multiplexed into eight data acquisition channels with a sampling frequency of 40 MHz and 12-bit precision.¹³ Due to the multiplexing, eight laser firings were required to generate a single 64-channel capture. Because the laser had 15-Hz repetition rate, the acquisition rate was about two frames per second.

The diffuse optical measurement system was a frequency-domain system and consisted of light source and detection subsystems, as well as a hand-held probe.²⁵ The source had four laser diodes of wavelengths 740, 780, 808, and 830 nm. Each laser diode was modulated at 140 MHz and sequentially coupled into six optical source fibers on the probe through optical switches. On the receiving end, the reflected light from the turbid medium associated with each of the illumination sources was detected simultaneously with 12 optical fiber bundles of 3 mm diameter. The detection fibers then coupled the light into 12 parallel photomultiplier tubes (PMTs) and electronics channels. An aluminum foil-covered plastic plate with dimensions of 9×10 cm was used for the hand-held probe as shown in Fig. 2(b). The middle slot was used for the ultrasound transducer, and the light source and detector fibers were deployed around the probe. The reflective aluminum foil prevented light from being absorbed by the probe and generating image artifacts.²⁸ Semi-infinite partial reflection boundary condition was used for the estimation of the background optical properties, and the aluminum cover provided an effective refraction coefficient of 0.6. In this study, the background optical properties obtained from the 780-nm laser diode only were used.

In the phantom experiments, 0.6% Intralipid solution was used to emulate the background breast tissue. The calibrated optical absorption coefficient (μ_a) and reduced scattering coefficient (μ'_s) of the Intralipid solution were in the range of 0.01 to 0.02 and 4.0 to 8.0 cm^{-1} , respectively, for the experiments. A 1 cm^{-3} -cubical soft absorber of higher ($\mu_a = 0.28 \text{ cm}^{-1}$), and another of lower ($\mu_a = 0.08 \text{ cm}^{-1}$) optical contrast was made from polyvinyl chloride plastisol and used to mimic a malignant and benign lesion respectively. The calibration was performed on a larger piece phantom of dimensions of $10 \times 10 \times 5 \text{ cm}^3$ using the DOM system. In general, a malignant lesion has higher contrast with optical absorption coefficient ranging from 0.18 to 0.4 cm^{-1} , and a benign lesion has the lower contrast with absorption coefficient from 0.007 to 0.15 cm^{-1} .²⁹⁻³¹

3 Results

3.1 Simulation Results with/without Background Optical Properties

Photoacoustic signals with 2% zero-mean Gaussian noise of a target of 1 cm diameter was simulated. In order to mimic breast lesions of different contrasts, the simulation was performed for different μ_a of the target ranging from 0.30 to 0.05 cm^{-1} in 0.05 cm^{-1} decrements and $\mu'_s = 7.0 \text{ cm}^{-1}$. The target was submerged in a scattering medium, having optical properties of $\mu_a = 0.02 \text{ cm}^{-1}$ and $\mu'_s = 7.0 \text{ cm}^{-1}$, and was located at the position ($x = 0, y = 0, z = 2.0$) cm relative to the center of the probe. If one assumes that the target location and size are already known from information obtained from the photoacoustic image, then there remain four unknowns: μ_a and μ'_s of the target, and μ_a and μ'_s of the background medium. Figure 3(a) and 3(b) are

the results from the four-parameter fitting. The solid lines in Fig. 3(a) represent the true μ_a value of the target (blue line) and background (black line), and the red stars and green squares are the fitted μ_a values for the target and background, respectively. The x -axis represents the expected target μ_a and background μ_a in cm^{-1} , and y -axis is the fitted μ_a in cm^{-1} . When the target has low contrast, such as 0.05 cm^{-1} , the error is largest: 102% for the fitted target μ_a , and 399% for the fitted background μ_a . On the other hand, as the target contrast gets higher, the errors gradually decrease to a minimum and then increase again as the contrast increases. The errors in the fitted target μ_a were 102%, 34%, 3.1%, 16.5%, 28.4%, and 36% corresponding to the target μ_a of 0.05, 0.10, 0.15, 0.20, 0.25, and 0.30 cm^{-1} , respectively. The fitted background μ_a decreased from 0.099 to 0.022 cm^{-1} when the target contrast increased from 0.05 to 0.30 cm^{-1} with the error ranging from 400% to 7%. Clearly, four-parameter fitting is not accurate enough to determine the target μ_a . This is because many unknowns can make the nonlinear fitting algorithm settle at the local minimum of the object function. Figure 3(b) shows the fitted results for the target μ'_s and background μ'_s with the error ranging from 12% to 27% for target μ'_s , and from 20% to 70% for background μ'_s . The fitted results for the case where the background μ_a and μ'_s are already known from DOM are shown in Fig. 3(c) and 3(d). It is seen from Fig. 3(c) that the errors for the fitted target μ_a have decreased to 4.6%, 1.2%, 0.7%, 0.55%, 0.5%, and 0.3% corresponding to the true target μ_a of 0.05, 0.10, 0.15, 0.20, 0.25, and 0.30 cm^{-1} , respectively. The errors for the fitted target μ'_s also ranged from 27% to 36%. Overall, the fitting accuracy for both the high and low contrast targets can be greatly improved if the total number of unknown parameters is decreased. Besides, the run-time of the fitting algorithm is also greatly reduced. This improvement was realized by using background optical properties obtained from the diffused optical measurements to reduce the four-parameter fitting to a two-parameter one. Figure 3(b) and 3(d) shows that the fitted target μ'_s is not very sensitive to the change in the background optical properties. As a result, the target μ_a is the only fitted parameter in the phantom experiments.

3.2 Phantom Experiments

The optical properties of the background medium can be calculated using Eqs. (3a) and (3b). Using the frequency domain diffuse optical measurement system described in Sec. 2.3, a set of amplitudes ($I_{\alpha\beta}$) and phases ($\phi_{\alpha\beta}$) is measured at different distances ($\rho_{\alpha\beta}$), where α represents the source number and β represents the detector number. Because the parameters for each PMT and individual laser diode varied considerably from one to another, we had to calibrate the gain and phase shift for each channel. Considering the gain difference and phase shift, Eq. (3) can be modified as

$$\log(\rho_{\alpha\beta}^2 I_{\alpha\beta}) = \log[I_s(\alpha)] + \log[I_d(\beta)] - k_i \rho_{\alpha\beta} \quad (5a)$$

$$\phi_{\alpha\beta} = \phi_s(\alpha) + \phi_d(\beta) + k_r \rho_{\alpha\beta}, \quad (5b)$$

where $I_s(\alpha)$ and $\phi_s(\alpha)$ are the relative gain and phase delay associated with source channel α , and $I_d(\beta)$ and $\phi_d(\beta)$ are similar quantities associated with detector channel β . k_r and k_i are the

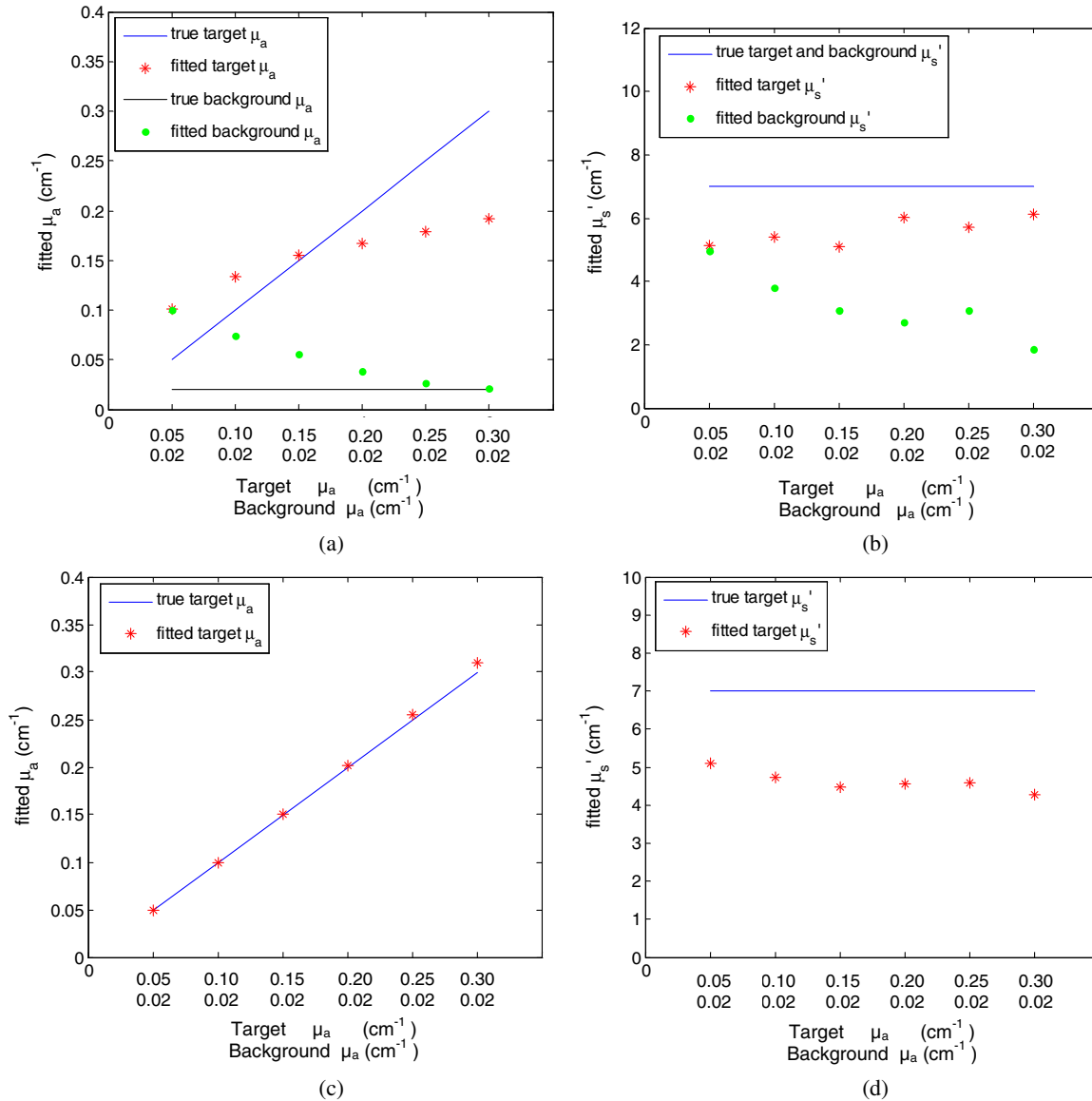


Fig. 3 Fitting results from the simulation data with 2% noise: (a) fitted background μ_a and target μ_a with four unknown parameters; (b) fitted background μ_s' and target μ_s' with four unknown parameters; (c) fitted target μ_a with two unknown parameters; (d) fitted target μ_s' with two unknown parameters.

real and imaginary parts of the complex wave number. In Eq. (5), the total number of unknowns are $2(\alpha + \beta) + 2$, which is far smaller than the total number of measurements $\alpha \times \beta$. Consequently, we can solve all the $I_s(\alpha)$, $\phi_s(\alpha)$, $I_d(\beta)$, and $\phi_d(\beta)$ terms.^{25,26} Figure 4(a) is an example of the calibrated amplitude [$\log(\rho_{\alpha\beta}^2 I_{\alpha\beta})$] versus source-detector distance in logarithmic scale, and Fig. 4(b) is an example of the calibrated phase versus s - d distances for 0.6% Intralipid solution, both at 780 nm. As one can see, the calibrated amplitude and phase from various pairs change linearly with distance. Therefore, the slopes of the two figures can be fitted as k_r and k_i , the real and imaginary parts of the complex wave number respectively. According to the diffusion theory, the complex wave number ($k = k_r + ik_i$) is related to the medium optical properties as²³

$$k^2 = \frac{3(-\nu\mu_a\mu_s' + i\omega\mu_s')}{\nu}, \quad (6)$$

where ν is the speed of light in the medium and ω is the modulation frequency. From this equation, μ_a and μ_s' can be solved

accordingly. The use of 0.4% to 0.8% Intralipid solutions always yielded scattering and absorption coefficients with rather good accuracy. The results in Fig. 4 were determined by using the source-detector distances between 2.5 and 5.5 cm, due to the sensitivity of the PMT. In this case, the background optical properties for 0.6% Intralipid solution were $\mu_a = 0.019 \text{ cm}^{-1}$ and $\mu_s' = 5.24 \text{ cm}^{-1}$ at 780 nm.

In the phantom experiments, the following calibration process was introduced to scale the simulation data to the measurements from the U.S. transducer array: we started with a phantom object with known optical properties, which was a 1- cm^3 cubical soft absorber made of polyvinyl chloride plastisol with the calibrated optical properties, $\mu_a = 0.30 \text{ cm}^{-1}$ and $\mu_s' = 6.2 \text{ cm}^{-1}$. An empirical relation, shown in Eq. (7), was established from PAT simulation trials of the phantom. The equation considered the scan angle of each transducer element in the simulation, and weighted the simulated pressure according to the distance of each pixel from the transducer elements as

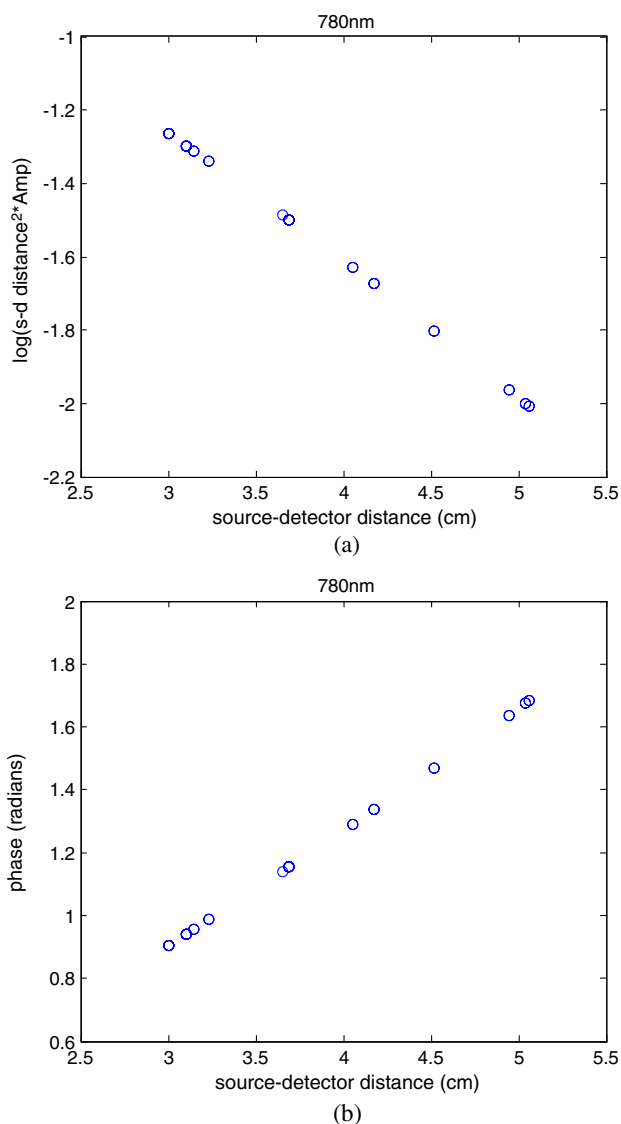


Fig. 4 Measured amplitude and phase profiles of diffuse waves: (a) $\log(\rho_{ap}^2 I_{ap})$ versus source-detector distances; (b) phases versus source-detector distances.

$$p(r, t) = \sum_{\Delta r} p_0[r(\theta) - \Delta r(\theta)] \cdot e^{-\frac{r(\theta)-s}{3.8}}, \quad (7)$$

where θ is the angle between the line joining a pixel to the transducer element and the vertical line through the element. Figure 5(a) compares the signal obtained from experiment with that from the simulation in one channel of the transducer. In this figure, the x -axis is the depth in units of mm, the y -axis is the amplitude of the signal in units of volts. The phantom center was located at 28 mm depth, and the front face at 23 mm depth. The red dash line in the figure is the PAT signal from experiment, and the blue solid line is that from simulation. It is seen that both the experimental and simulated signals closely match each other in terms of the target location and generated acoustic amplitude. At the shallower depth, however, the mismatch between the simulated and experimental data was high. This is because in the experimental data, photoacoustic signals generated from the transducer's front face upon light illumination were present.^{28,32} On the other hand, this signal

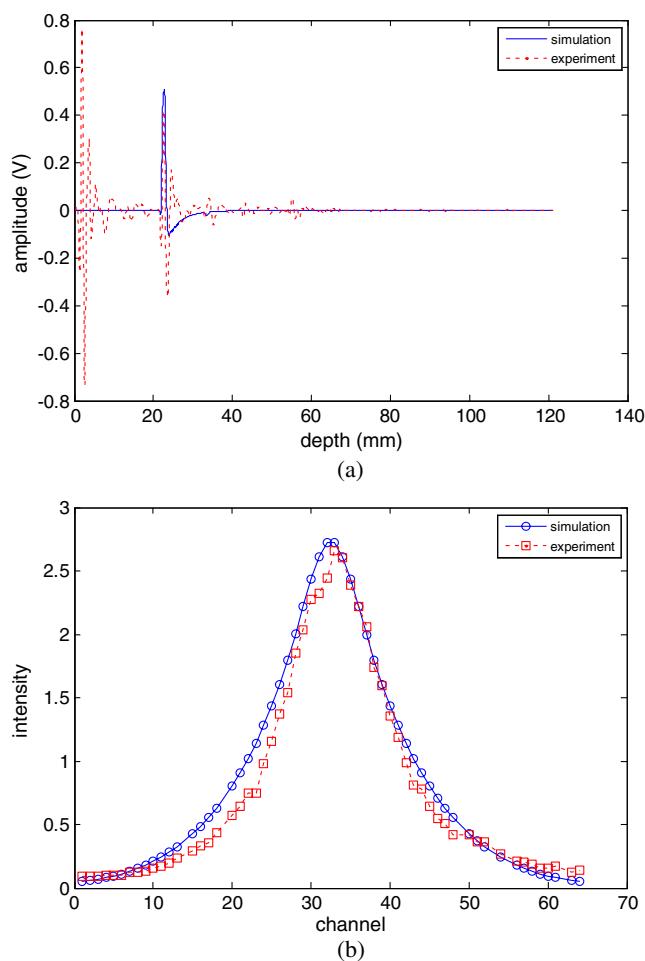


Fig. 5 Comparison of the experimental and simulated signals: (a) experimental signal and simulated signal obtained from one U.S. transducer element; (b) the total intensities obtained from experimental signals and simulation signals from 64 channels.

was absent in the simulated data. However, this does not pose any problem as the fitting procedure only compares the difference between the experimental and simulated signals at the region around the target. In the case of Fig. 5(a), the signals from depths of 18 to 40 mm were summed up for each channel, as shown in Fig. 5(b). The x -axis represents the 64 elements of the transducer; the y -axis is the summation of the amplitude signal from each channel. The red dash line represents the experimental signal, whereas the blue solid line represents the simulation. The shape and amplitude of these two curves compare favorably well with each other. The calibrations were performed at different depths and used in the experiments.

A 1 cm³-cubical absorber of higher ($\mu_a = 0.28 \text{ cm}^{-1}$) and another of lower ($\mu_a = 0.08 \text{ cm}^{-1}$) optical contrast were used as soft tissue targets to mimic a high-contrast malignant lesion and low-contrast benign lesion, respectively. The absorber was placed inside Intralipid with calibrated optical properties of $\mu_a = 0.019 \text{ cm}^{-1}$ and $\mu_s' = 5.24 \text{ cm}^{-1}$, and imaged at depths of 1.5, 2.0, 2.5, and 3.0 cm measured from the transducer face to the center of the absorber. Figure 6(a) shows the PAT images of the higher-contrast target with its center located at 2.0 cm from the transducer. The horizontal axis of the PAT images is the lateral dimension (in mm) in the x -direction, and the vertical axis is the depth (in mm) in the z -direction.

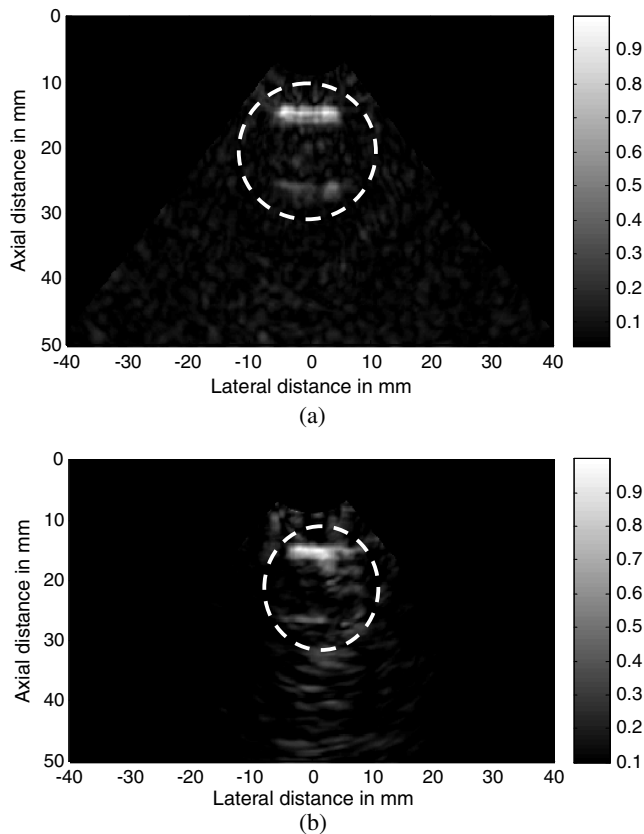


Fig. 6 (a) PAT images of the high contrast target with center located at 2.0 cm depth; (b) PAT images of the low contrast target with center located at 2.0 cm depth. The x-axis of the PAT images is lateral dimension and vertical z-axis is the depth. The units are mm. The circled region shows the cubic target.

The high-resolution PAT images clearly delineate the front and back face of the target, as shown in the circled regions in the figure. The location of the target can be read as (0.2, 2.0) cm in x and z directions. Because the photoacoustic images provided only a two-dimensional (2-D) image, the center of the target in the y dimension was set to $y = 0$, which is the center of the transducer [as shown in Fig. 2(b)]. The fitted target μ_a converged to 0.255 cm^{-1} after 18 iterations, which was 91% of the true value. Table 1 lists the fitted results and errors for the higher-contrast absorber at different depths. The errors in the fitted data range from 7.1% to 16.8%; these are 18% to 37% better than the reconstructed DOT results with guidance from PAT image in Ref. 14. In the referenced paper, the maximum

reconstructed absorption coefficients for the higher-contrast target have errors about 25% to 54%.

Similar experiments were performed for the lower-contrast target. Figure 6(b) shows the PAT images of this target whose center location may be read as $(-0.5, 2.0)$ cm. The contrast of the PAT images was not as good as that of the higher-contrast one. However, the front and back faces of the target were fairly resolved. After 14 iterations, the fitted target μ_a had a final converged value of 0.086 cm^{-1} , which is 108% of the true value. The fitting results at other depths are listed in Table 1, and the errors at different depths range from 3.8% to 11.2%. These values are either comparable or 20% better than the DOT results for low contrast target in Ref. 14.

3.3 Sensitivity Test

The sensitivity of the two-parameter fitting procedure to the target parameters and background optical properties was evaluated. We found that accurate target information, namely the location (x, y, z) and size, are critical for the fitting procedure. As shown in Fig. 7(a), where the x -axis is the measured radius of target and y -axis is the fitted μ_a in cm^{-1} , if the target's radius is not estimated accurately, varying from 0.4 to 0.6 cm, the fitted μ_a is greatly influenced by this error. This is easy to understand because the total signal is related to the volume of the target. When the estimated target size is smaller than that of true size, the fitted absorption coefficient increases to match the measured signal; in this case, the errors increase from 15% to 74%. An example of this is shown in Fig. 7(a) for a target centered at 2.5 and 3.0 cm, and in general is true for all depths. The fitted μ_a is also strongly related to the target depth as shown in Fig. 7(b). In this figure, the x -axis is the assumed target depth, and we still used the data in which the target was centered at 2.5 and 3.0 cm depths. When the target depth input is not accurate, the fitted error also increases from 15% to 100%. On the other hand, the x - y location of target has small influence on the fitting accuracy as shown in Fig. 7(c). The x -axis represents the target location in the x direction, and y -axis represents the fitted target μ_a values. When the location of the target was moving in the x -direction away from the true location up to 0.2 cm, the fitted μ_a varied less than 7%.

The background optical properties are also critical to the two-parameter fitting procedure. Figure 8(a) shows that the target fitted μ_a changes as the input background μ_a increases. In the figure, the x -axis represents the background μ_a in cm^{-1} , and y -axis is the fitted μ_a . The error ranges from 16% to 45%. The background μ_s' also has similar influence on the fitting procedure as shown in Fig. 8(b). In this figure, x -axis represents the background μ_s' , and y -axis is the fitted target μ_a . When the

Table 1 Phantom experiment for single high-contrast target (calibrated $\mu_a = 0.28 \text{ cm}^{-1}$) and low-contrast target (calibrated $\mu_a = 0.08 \text{ cm}^{-1}$).

Reconstructed μ_a (cm^{-1})	High-contrast target		Low-contrast target	
	Fitted value	Error	Fitter value	Error
Target center depth 1.5 cm	0.300	7.1%	0.083	3.8%
Target center depth 2.0 cm	0.255	8.9%	0.086	7.5%
Target center depth 2.5 cm	0.233	16.8%	0.071	11.2%
Target center depth 3.0 cm	0.255	10.7%	0.075	6.2%

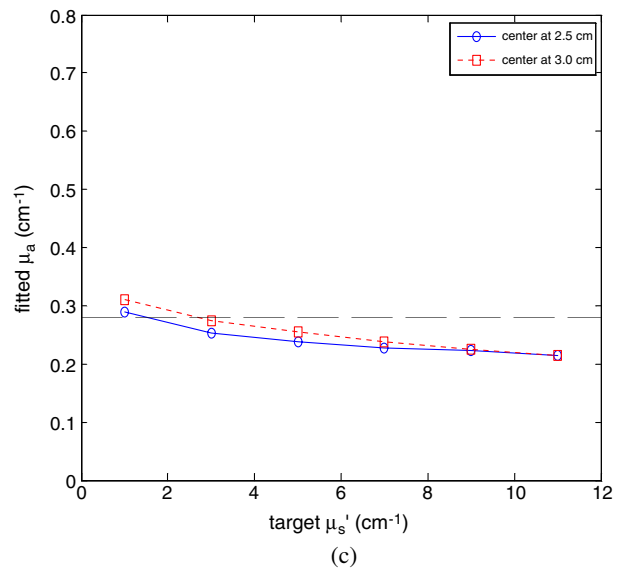
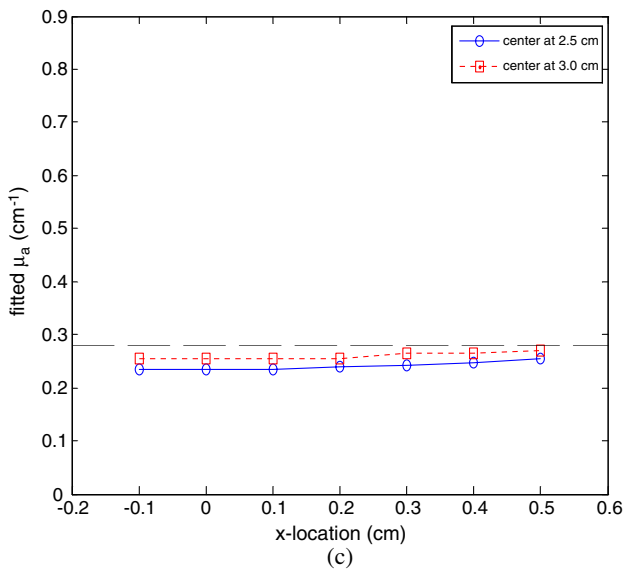
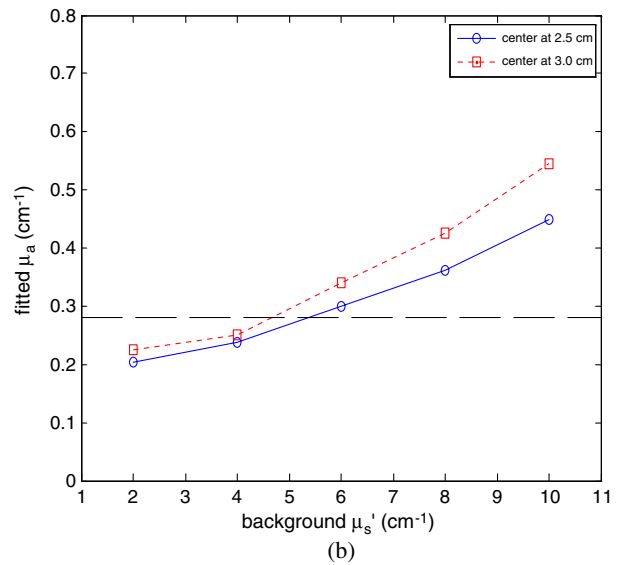
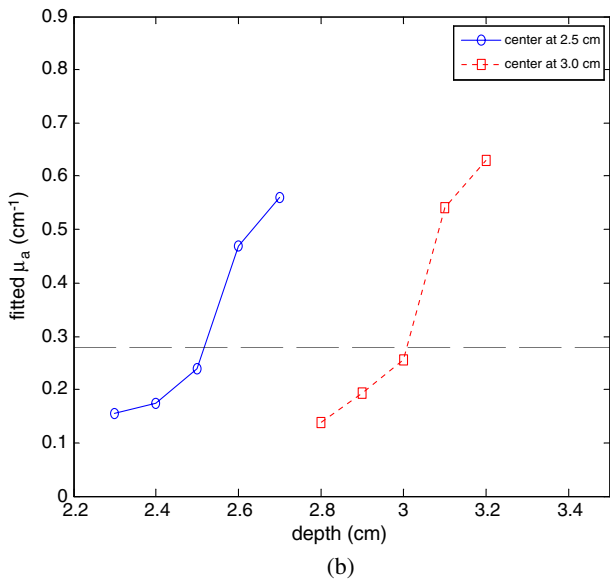
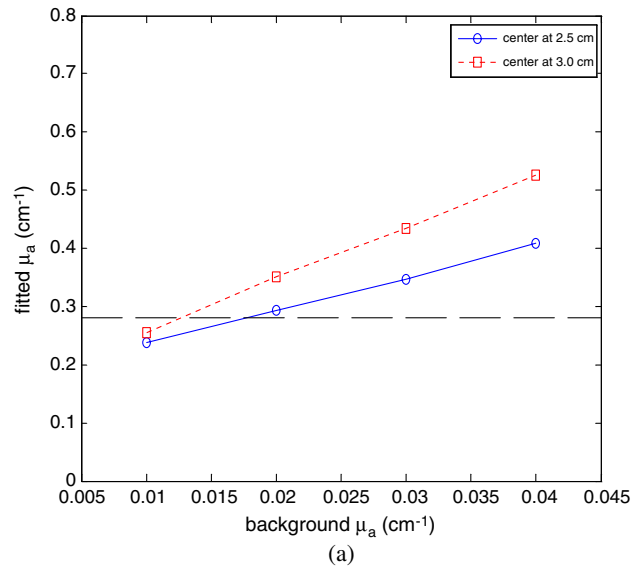
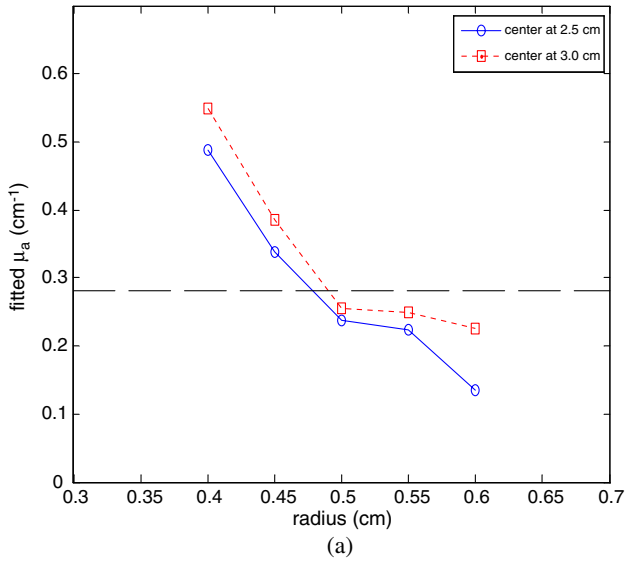


Fig. 7 The influence of structural information: (a) radius; (b) depth; (c) x-y plane.

Fig. 8 The influence of optical properties: (a) background μ_a change; (b) background μ_s' change; (c) target μ_s' change.

background μ'_s is not accurate, the fitting error also increases from 16% to 60%. On the other hand, the target μ'_s has a small influence on the fitting accuracy as shown in Fig. 8(c). The x -axis represents the target μ'_s and ranges from 1 to 11 in 2 cm^{-1} increments, and y -axis represents the fitted target μ_a . When the target μ'_s was changed, the fitted μ_a varied less than 20%.

3.4 Blood Tube Experiments

To test the robustness of the fitting procedure, we also performed experiments with blood collected from a sacrificed mouse. The blood was diluted and injected into a thin tube with 0.58-mm inner diameter and 0.9-mm outer diameter. To estimate the absorption coefficient of the blood, the formula from Ref. 33 was used.

$$\mu_a(\lambda) = 2.303 e(\lambda) \cdot C / (64500 \text{ g Hb/mole}), \quad (8)$$

where $e(\lambda)$ is molar extinction coefficient and C is the diluted hemoglobin concentration of the blood. From the hemoglobin concentration, the calculated μ_a is 0.39 cm^{-1} . Figure 9 shows the PAT image of the blood tube that is submerged inside Intralipid with optical properties of $\mu_a = 0.02 \text{ cm}^{-1}$ and $\mu'_s = 4.9 \text{ cm}^{-1}$ at a depth of 1.5 cm. The converged value for μ_a was 0.342 cm^{-1} ; this is 88% of estimated true value.

4 Summary and Discussion

Currently, ultrasound (US) is used extensively as an adjunct to x-ray mammography to differentiate cysts from solid lesions and is increasingly used for screening younger patients. However, ultrasound probes mechanical contrast of the lesion. On the other hand, PAT provides functional information of the lesion related to light absorption of hemoglobin content. Due to the different contrast mechanisms, some lesions may not be detectable by a nonoptical modality but yet have high optical contrast. A single contrast usually cannot provide accurate diagnosis because of biological variability. As a result, the combination of PAT and DOM or DOT may likely improve the detection and diagnosis of US occult lesions.

Diffuse optical measurements have shown to provide reliable background optical properties of breast tissue.^{34,35} For patients with breast lesions, the background optical properties can be measured from the contralateral breasts. Photoacoustic techniques have shown promising results to map breast tissue optical

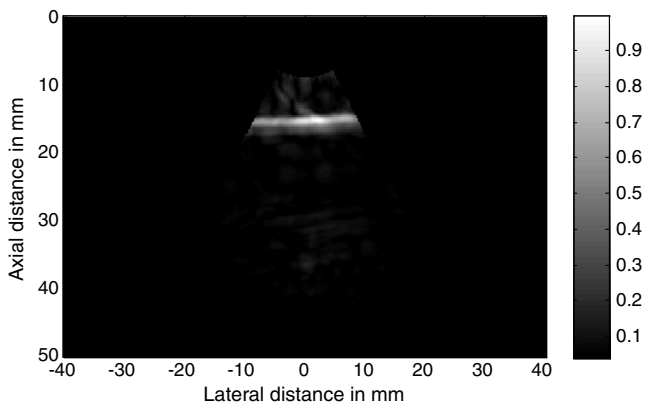


Fig. 9 PAT image of the blood tube.

absorption contrast with ultrasound resolution, which is an order of magnitude higher than that of diffuse optical tomography. However, quantitative optical contrast is not readily available by photoacoustic tomography. This study demonstrates that diffuse optical measurements can assist photoacoustic tomography in quantifying target optical contrast by iteratively fitting the forward model with the experimental data. The forward model using the analytical expression for fluence in the medium and photoacoustic wave propagation is faster in terms of computation, when compared with the finite element method.

There are still technical challenges that need to be solved before *in vivo* studies become feasible. First, the accurate quantification of the target depends on the accurate estimation of target diameter and depth, which in turn depends on the image quality of the photoacoustic images. Since we do not have clinical examples of photoacoustic imaging yet, we used existing ultrasound images obtained from breast lesions of patients to estimate the potential error in future PAT clinical experiments. This is acceptable because photoacoustic and ultrasound images have similar resolutions, albeit different contrasts. Figure 10(a) is an ultrasound image of a benign lesion of a 53-year-old patient obtained prior to her ultrasound-guided core biopsy [case 1 in Fig. 10(b)]. An ultrasound expert marked the boundary of the lesion and estimated the depth of the lesion. In general, the depth of the lesion is

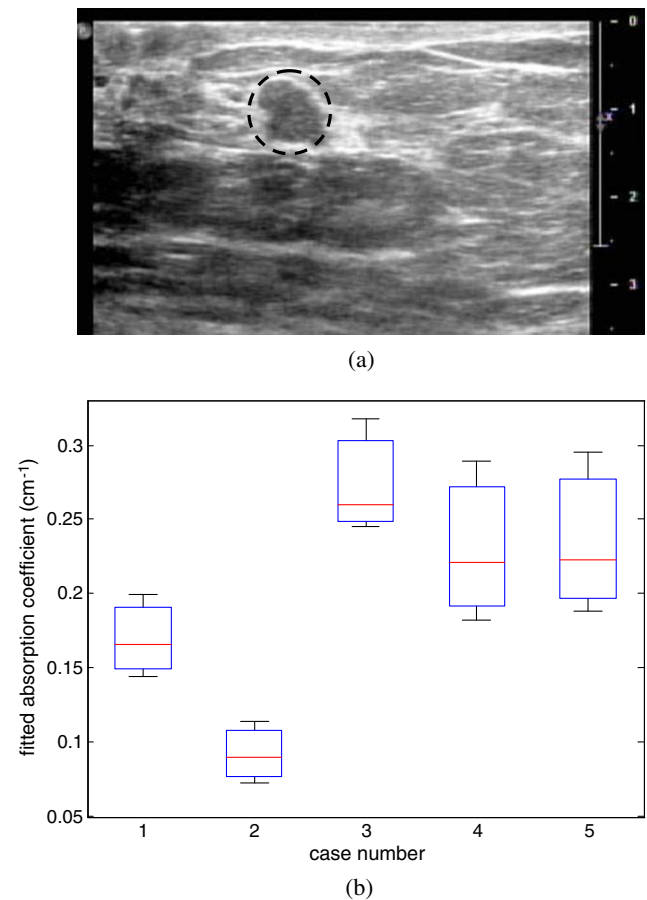


Fig. 10 Simulation of the potential target-size effects on optical contrast quantification using target-size measurements obtained from clinical ultrasound images: (a) ultrasound image with marked boundary obtained from a 53-year-old woman; (b) the box and whisker plot of the maximum absorption of the lesions.

relatively accurate, but the radius is more subjective. However, for smaller lesions in the neighborhood of 1 cm, the estimated radii are typically within 80% to 120% of the true size. This is based on our experience obtained from correlating sizes measured from ultrasound images and tumor stages reported from surgical pathology. Accordingly, in the simulation, the measured radius, together with 80% and 120% of it, were used in the fitting procedure, which represented 64% to 144% of the area of interest. The fitting results for five cases are plotted in Fig. 10(b). The first two cases were benign fibroadenoma, and the last three cases were malignant carcinoma. Clearly, the radius changes have influence on the fitting value, but the benign and malignant lesions can be separated. To further improve the photoacoustic imaging capability on delineating tumor margins, contrast agents may be needed to reliably identify the target parameters.

Second, the ultrasound transducer face generates photoacoustic waves upon the absorption of light from source fibers. These waves propagate to the target where they are reflected back to the transducer and picked up as signals, producing artifacts in the photoacoustic images; these artifacts are especially prominent in the low-contrast target images. We have been evaluating different type of materials that can be used at the face of the ultrasound transducer to effectively prevent light absorption and at the same time minimize the acoustic signal attenuation.²⁸ Third, the current system is not portable for clinical experiment. In the current setup, the light is delivered through two 1000-micron step-index fibers, and the output energy density is about 80 mJ/cm² which exceed the ANSI safety standard (20 mJ/cm²). We are looking for a compact laser and have cooperation with OFS Inc., which is developing a new fiber assembly using a proprietary power splitting technology to split light energy from one 940-micron core input fiber to nineteen 200-micron core output fibers. The fiber assembly will decrease the energy density output of the source fibers by a factor of 10. Fourth, the current fitting procedure is suitable for a single target. In principle, this method can be extended to multiple-target scenarios by taking care of cross-talk signals between targets; we are currently investigating several fitting procedures to address this issue.

In summary, we have presented a new fitting method, which can quantitatively recover the absorption coefficient using a diffuse optical measurements-assisted photoacoustic tomography in reflection geometry. The background optical properties provided by the diffuse measurements can reduce the total unknowns in the fitting procedure and significantly improve the target characterization. This hybrid technique may overcome challenges and limitations of each technology alone and has potential in cancer detection and diagnosis.

Acknowledgments

The authors thank the National Institute of Health (R01EB002136), and Army Medical Research and Materiel Command Postdoctoral Fellowship award (W81XWH-09-1-0511), for funding and supporting this work.

References

1. X. Wang et al., "Noninvasive laser-induced photoacoustic tomography for structural and functional in vivo imaging of the brain," *Nat. Biotechnol.* **21**(7), 803–806 (2003).
2. L. V. Wang, "Prospects of photoacoustic tomography," *Med. Phys.* **35**(12), 5758–5767 (2008).
3. G. Ku et al., "Thermoacoustic and photoacoustic tomography of thick biological tissues toward breast imaging," *Technol. Cancer Res. Treat.* **4**(5), 559–565 (2005).
4. D. Razansky, C. Vinegoni, and V. Ntziachristos, "Imaging of mesoscopic targets using selective-plane photoacoustic tomography," *Phys. Med. Biol.* **54**(9), 2769–2777 (2009).
5. K. H. Song et al., "Noninvasive photoacoustic identification of sentinel lymph nodes containing methylene blue *in vivo* in a rat model," *J. Biomed. Opt.* **13**(5), 054033, (2008).
6. S. Ermilov et al., "Laser opto-acoustic imaging system for detection of breast cancer," *J. Biomed. Opt.* **14**(2), 024007, (2009).
7. H. Brecht et al., "Whole-body three-dimensional optoacoustic tomography system for small animals," *J. Biomed. Opt.* **14**(6), 064007, (2009).
8. E. Zhang, J. Laufer, and P. Beard, "Backward-mode multiwavelength photoacoustic scanner using a planar Fabry-Perot polymer film ultrasound sensor for high-resolution three-dimensional imaging of biological tissues," *Appl. Opt.* **47**(4), 561–577 (2008).
9. J. Laufer et al., "Three-dimensional noninvasive imaging of the vasculature in the mouse brain using a high resolution photoacoustic scanner," *Appl. Opt.* **48**(10), 299–306 (2009).
10. D. Piras et al., "Photoacoustic imaging of the breast using the twente photoacoustic mammoscope: present status and future perspectives," *IEEE J. Sel. Top. Quantum Electron* **16**(4), 730–739 (2010).
11. V. G. Andreev et al., "Opto-acoustic tomography of breast cancer with arc-array transducer," *Proc. SPIE* **3916**, 36–47 (2000).
12. A. Oraevsky et al., "Laser opto-acoustic imaging of breast cancer *in vivo*," *Proc. SPIE* **4256**, 6–15 (2001).
13. J. Gamelin et al., "Photoacoustic guidance of diffusive optical tomography with a hybrid reflection geometry probe," *Proc. SPIE* **7177**, 0701–0711 (2009).
14. P. D. Kumavor et al., "Target detection and quantification using a hybrid hand-held diffusive optical tomography and photoacoustic tomography system," *J. Biomed. Opt.* **16**(4), 046010, 1–12 (2011).
15. Z. Yuan and H. Jiang, "Quantitative photoacoustic tomography: recovery of optical absorption coefficient of heterogeneous media," *Appl. Phys. Lett.* **88**(23), 213301(2006).
16. Z. Yuan, Q. Wang, and H. Jiang, "Reconstruction of optical absorption coefficient maps of heterogeneous media by photoacoustic tomography coupled with diffusion equation based regularized Newton method," *Opt. Express* **15**(26), 18076–18081 (2007).
17. L. Yin et al., "Tomographic imaging of absolute optical absorption coefficient in turbid media using combined photoacoustic and diffusing light measurements," *Opt. Lett.* **32**(17), 2556–2558 (2007).
18. J. Laufer et al., "Quantitative spatially resolved measurement of tissue chromophore concentrations using photoacoustic spectroscopy: application to the measurement of blood oxygenation and haemoglobin concentration," *Phys. Med. Biol.* **52**(1), 141–168 (2007).
19. J. Laufer, E. Zhang, and P. Beard, "Evaluation of absorbing chromophores used in tissue phantoms for quantitative photoacoustic spectroscopy and imaging," *IEEE J. Sel. Top. Quantum. Electron.* **16**(3), 600–608 (2010).
20. A. Rosenthal, D. Razansky, and V. Ntziachristos, "Quantitative opto-acoustic signal extraction using sparse signal representation," *IEEE Trans. Med. Imag.* **28**(12), 1997–2006 (2009).
21. R. Zemp, "Quantitative photoacoustic tomography with multiple optical sources," *Appl. Opt.* **49**(18), 3566–3572 (2010).
22. Z. Guo, S. Hu, and L. Wang, "Calibration-free absolute quantification of optical absorption coefficients using acoustic spectra in 3-D photoacoustic microscopy of biological tissue," *Opt. Lett.* **35**(12), 2067–2069 (2010).
23. D. Boas et al., "Scattering of diffuse photon density waves by spherical inhomogeneities within turbid media—analytic solution and applications," *Proc. Natl. Acad. Sci. USA* **91**(11), 4887–4891 (1994).
24. K. Kostli et al., "Temporal backward projection of opto-acoustic pressure transients using Fourier transform methods," *Phys. Med. Biol.* **46**(7), 1863–1872 (2001).
25. Q. Zhu et al., "Optimal probing of optical contrast of breast lesions of different size located at different depths by US localization," *Technol. Cancer Res. Treat.* **5**(4), 365–380 (2006).
26. N. G. Chen et al., "Simultaneous near infrared diffusive light and ultrasound imaging," *Appl. Opt.* **40**(34), 6367–6280 (2001).

27. C. Hoelen and F. de Mul, "Image reconstruction for photoacoustic scanning of tissue structures," *Appl. Opt.* **39**(31), 5872–5883 (2000).
28. B. Tavakoli et al., "Effect of ultrasound transducer face reflectivity on the light fluence inside a turbid medium in photoacoustic imaging," *J. Biomed. Opt.* **15**(4), 046003 (2010).
29. Q. Zhu et al., "The potential role of optical tomography with ultrasound localization in assisting ultrasound diagnosis of early-stage invasive breast cancers," *Radiology* **256**(2), 367–378 (2010).
30. Q. Zhu et al., "Ultrasound-guided optical tomographic imaging of malignant and benign breast lesions: initial clinical results of 19 cases," *Neoplasia* **5**(5), 379–388 (2003).
31. D. Grosenick et al., "Time-domain scanning optical mammography: Optical II. properties and tissue parameters of 87 carcinomas," *Phys. Med. Biol.* **50**(11), 2451–2468 (2005).
32. P. D. Kumavor, A. Aguirre, and Q. Zhu, "Reduction of secondary echoes generated from ultrasound transducer face in photoacoustic imaging implemented in reflection geometry," in *Biomed. Opt., OSA Technical Digest (CD)* (Optical Society of America, 2010), paper BSuD7. <http://omlc.ogi.edu/spectra/hemoglobin/>.
33. <http://omlc.ogi.edu/spectra/hemoglobin/>.
34. N. Shah et al., "Noninvasive functional optical spectroscopy of human breast tissue," *Proc. Natl. Acad. Sci* **98**(8), 4420–4425 (2001).
35. T. Durduran et al., "Bulk optical properties of healthy female breast tissue," *Phys. Med. Biol.* **47**(16), 2847–2861 (2002).